

Article

Schwartz Symmetry Condition for Coherent Diffraction Imaging Patterns

Eduardo X. Miqueles ^{*}, Tiago Kalile and Yuri R. Tonin 

Brazilian Synchrotron Light Laboratory, The Brazilian Center for Research in Energy and Materials, Campinas 13083-100, SP, Brazil; tiago.kalile@lnls.br (T.K.); yuri.tonin@lnls.br (Y.R.T.)

* Correspondence: eduardo.miqueles@lnls.br

Abstract: We demonstrate a symmetry condition for the mixed partial derivatives of measured data when performing a coherent diffraction imaging (CDI) experiment for differentiable samples under scientific investigation. The proposed condition can be used as a physical restriction to improve real data measurements and has been used within the most celebrated phase-retrieval inversion algorithms as an ad hoc constraint without proof. The symmetry relies on John's ultrahyperbolic equation for the X-ray transform, which is also demonstrated to be valid in the imaging regime for CDI. The obtained conditions are easy to implement and can be used as a constraint by computational imaging methods.

Keywords: inverse problems; diffraction; symmetry; imaging; synchrotron

1. Introduction

Coherent diffractive imaging (CDI) has been steadily developing over the past 20 years [1], and its variants greatly benefit from the high coherence of fourth-generation light sources [2–4]. These techniques, in principle, allow experiments to achieve resolutions on the order of a few nanometers, greatly increasing the potential for scientific exploration in biological and materials science. Nonetheless, data acquisition is only one of the challenges in CDI. Since these techniques rely on computational methods for phase retrieval, which is generally an ill-posed problem, the quality of the measured data becomes a bottleneck for successful image reconstruction.

Usually, careful pre-processing of measured diffraction data is required prior to feeding it to phase-retrieval algorithms such as error reduction (ER), hybrid input–output (HIO) [5], and oversampling smoothness (OSS) [6]. For instance, flat-field correction and masking of dead and hot pixels are crucial for phase-retrieval algorithms to converge, especially when bad pixels alter the information in the low-frequency region of diffraction patterns [7]. Detection of these bad pixels is usually performed manually with the aid of visualization software, which is a time-consuming and cumbersome process. Hence, the development of methods to automatically detect corrupted pixels not only helps increase the data quality but also expedites the processing pipelines for obtaining high-resolution images. We also emphasize that pixel detection is a conventional task that can be solved with conventional image processing tools [8]. However, these tools normally make use of the hypothesis that outlier pixels have constant intensity, which is not the case with diffraction patterns in the applications presented and discussed in this manuscript. Here, we classify outlier pixels as "hot" and "warm" in the sense that there exists photon counting in these pixels, which varies randomly and must be automatically corrected. For this, we use the symmetry condition satisfied by the measured image, as demonstrated in this manuscript. Further imaging modalities in different imaging regimes, as is the case of infrared holography [9], can also present errors in background intensity measurement, which also need to be corrected.



Citation: Miqueles, E.X.; Kalile, T.; Tonin, Y.R. Schwartz Symmetry Condition for Coherent Diffraction Imaging Patterns. *Symmetry* **2024**, *16*, 399. <https://doi.org/10.3390/sym16040399>

Academic Editors: Keke Shang and Qunli Lei

Received: 25 January 2024

Revised: 21 March 2024

Accepted: 22 March 2024

Published: 29 March 2024



Copyright: © 2024 by the authors. Licensee MDPI, Basel, Switzerland. This article is an open access article distributed under the terms and conditions of the Creative Commons Attribution (CC BY) license (<https://creativecommons.org/licenses/by/4.0/>).

2. X-ray Transform

The X-ray projection for an absorbing sample can be approximately described by the Beer–Lambert (BL) absorption law [10]. Under certain physical circumstances, imaging practitioners deal with a function $F: \mathbb{R}^3 \times \mathbb{R}^3 \rightarrow \mathbb{R}$ that is theoretically determined by the so-called X-ray transform [11]

$$F(x, y) = \int_{\mathbb{R}} f(x + t(y - x)) dt, \quad (1)$$

where $x, y \in \mathbb{R}^3$ are points outside the support of function f , usually defined as the linear absorption coefficient that determines the inverse problem the experiment is investigating. Under an appropriate change of coordinates, F denotes the so-called Radon transform, and whenever parameterized at a constant surface, F is denoted as a frame, a radiography, or a projection, which includes several experimental artifacts as well as noise. Some of these artifacts are extremely problematic, leading to reconstruction artifacts in the inverse problem. Function F is a solution of John's equation [11], an ultrahyperbolic partial differential equation, which is given by

$$\frac{\partial^2 F}{\partial x_i \partial y_j} - \frac{\partial^2 F}{\partial y_i \partial x_j} = 0, \quad i, j = 1, 2, 3 \quad (2)$$

In practice, F is measured for a collection of source and receiver pairs $y, x \in \mathbb{R}^3$ such that the vector $x - y$ is parallel to the X-ray wavefront propagation (see Figure 1). At the end of this process, one can obtain a two-dimensional discretization of F on an $m \times n$ grid on the receiver plane, where m and n depend on the number of scanning points or the size of the detector being used. For most imaging techniques using X-rays, the practical measurements are the functions $I(x)$ (direct transmission) and $I^0(y)$ (incident transmission) in such a way that $F(x, y)$ satisfies $I(y) = I^0(y) \exp[-F(x, y)]$.

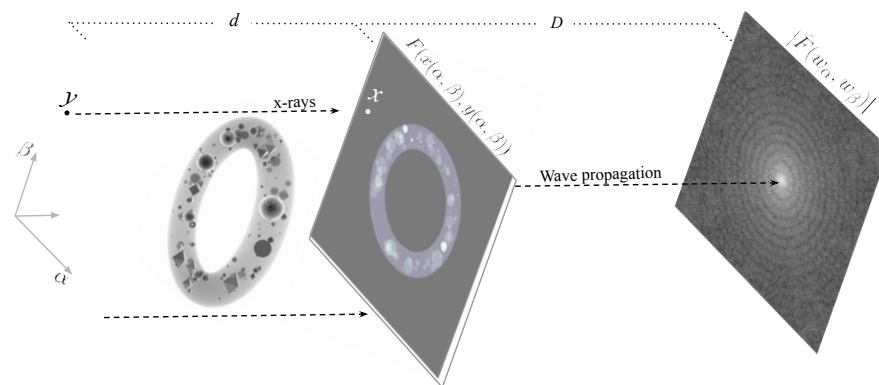


Figure 1. Scanning measurements for all points $y, x \in \mathbb{R}^3$ such that $y - x$ is parallel to the X-ray direction, generating a radiographic projection F . After wave propagation for long distances D , the measurement becomes $|\hat{F}|$.

Regardless of the imaging technique used, F is corrupted, and a fast and stable algorithm must be used to identify the points (or pixels) where the projection is corrupted. A numerical framework for this task was recently obtained for conic projections [12] or using source helicoidal trajectories [13]. A more theoretical and generalized analysis can be found in [14]. Nonetheless, for a parallel beam, a numerical analysis is lacking in the literature. In the next sections, we demonstrate a symmetry condition that must be satisfied by the X-ray transform and the equivalence of such a condition to a numerical operator. The direct application of this operator to corrupted projections or diffraction data turns out to be an efficient tool for identifying bad pixels, which we demonstrate with CDI data acquired from the CATERETÉ beamline at SIRIUS.

3. Symmetry Condition

Our main result is based on Lemma 1, which states that the projection image, parameterized as a function of α, β in the detector plane, should satisfy the Schwartz symmetry condition (or Young's theorem). Since this is a weak condition to impose on a function of two variables, an alternative condition on the parameterized function is proposed based on the characteristic polynomial of its associated Hessian matrix.

Lemma 1. Let $h: \mathbb{R}^2 \rightarrow \mathbb{R}$ be an arbitrary $C^2(\mathbb{R}^2)$ function. The X-ray transform F defined in (1), parametrized on the imaging plane $\alpha \times \beta$ and considering a parallel beam, determines a function $u(\alpha, \beta) = F(x(\alpha, \beta), y(\alpha, \beta))$ that must satisfy the symmetry condition for mixed second derivatives

$$\mathcal{J}(u) := \frac{\partial^2 u}{\partial \beta \partial \alpha} - \frac{\partial^2 u}{\partial \alpha \partial \beta} = 0 \quad (3)$$

Throughout this work, and whenever necessary, the notation $u_{\alpha, \beta}$ is used to indicate the mixed second derivative, first with respect to β , followed by a derivative with respect to α .

The detection surface used in Lemma 1 could be any differentiable function of two variables. In practice, one can consider it a plane since we are dealing with an ideal X-ray transmission. The three-dimensional point source y and the detector point x , which define the X-ray transform, belong to different planes separated by a distance d greater than the object being illuminated. Taking x on a three-dimensional surface $h = h(\alpha, \beta)$, we consider that $x = (\alpha, \beta, h(\alpha, \beta))$ and $y = (\alpha, \beta, 0) \in \mathbb{R}^3$. Now, the X-ray transform F becomes a function only of (α, β) , denoted as $u(\alpha, \beta)$, i.e.,

$$u(\alpha, \beta) = F(\underbrace{(\alpha, \beta, h(\alpha, \beta))}_x, \underbrace{(\alpha, \beta, 0)}_y) \quad (4)$$

From the chain rule, we can immediately obtain the mixed second derivative of u with respect to β , that is,

$$\frac{\partial^2 u}{\partial \beta \partial \alpha} = \left(\frac{\partial^2 F}{\partial x_2 \partial x_1} + \frac{\partial^2 F}{\partial x_2 \partial x_3} h_\alpha + \frac{\partial^2 F}{\partial x_2 \partial y_1} \right) + \left(\frac{\partial^2 F}{\partial x_3 \partial x_1} + \frac{\partial^2 F}{\partial x_3 \partial x_3} h_\alpha + \frac{\partial^2 F}{\partial x_3 \partial y_1} \right) h_\beta + \left(\frac{\partial^2 F}{\partial y_2 \partial x_1} + \frac{\partial^2 F}{\partial y_2 \partial x_3} h_\alpha + \frac{\partial^2 F}{\partial y_2 \partial y_1} \right) \quad (5)$$

and also the mixed second derivative of u with respect to α ,

$$\frac{\partial^2 u}{\partial \alpha \partial \beta} = \left(\frac{\partial^2 F}{\partial y_1 \partial x_2} + \frac{\partial^2 F}{\partial y_1 \partial x_3} h_\beta + \frac{\partial^2 F}{\partial y_1 \partial y_2} \right) + \left(\frac{\partial^2 F}{\partial x_3 \partial x_2} + \frac{\partial^2 F}{\partial x_3 \partial x_3} h_\beta + \frac{\partial^2 F}{\partial x_3 \partial y_2} \right) h_\alpha + \left(\frac{\partial^2 F}{\partial x_1 \partial x_2} + \frac{\partial^2 F}{\partial x_1 \partial x_3} h_\beta + \frac{\partial^2 F}{\partial x_1 \partial y_2} \right) \quad (6)$$

Therefore, using (5) and (6), the following result is obtained

$$\mathcal{J}(u) = 2 \left(\frac{\partial^2 F}{\partial x_2 \partial y_1} - \frac{\partial^2 F}{\partial y_1 \partial x_2} \right) + h_\beta \left(\frac{\partial^2 F}{\partial x_3 \partial y_1} - \frac{\partial^2 F}{\partial y_1 \partial x_3} \right) + h_\alpha \left(\frac{\partial^2 F}{\partial y_2 \partial x_3} - \frac{\partial^2 F}{\partial x_3 \partial y_2} \right), \quad (7)$$

which should vanish for all possible values of α, β as an immediate consequence of John's Equation (2), concluding the proof for Lemma 1.

The practical case: Let I and I^0 denote the transmitted and incident photon counts on the pixel camera, respectively, parameterized by the point (α, β) and for a particular angle θ . If the sample is placed between the source and detector surface in such a way that the projection image I is well determined by the Beer–Lambert (BL) law (8), we expect that $I < I^0$ for all possible points (α, β) on the detector surface. Unfortunately, sometimes this is not true in real measurements due to several physical properties (e.g., the paraxial wave propagation inside the object could carry information from nearby voxels through the ideal propagated X-ray, causing a large photon count that is greater than the expected incoming measurement); hence, the logarithm cannot be applied in points where $I > I^0$. Under

physical assumptions that are beyond the scope of this work, the photon propagation through a sample obeys the BL law [10]

$$I(\alpha, \beta) = I^0(\alpha, \beta)e^{-u_m(\alpha, \beta)} \quad (8)$$

where u_m is an idealization of F (see Equation (1)). Considering (8), a simple calculation provides the following result

$$\mathcal{J}(u_m) = \mathcal{J}(I)/I + e^{-u_m} \mathcal{J}(I^0)/I \quad (9)$$

where \mathcal{J} is the operator described in Lemma 1. Here, we can clearly see that $\mathcal{J}(u_m) = 0$ only if $\mathcal{J}(I) = \mathcal{J}(I^0) = 0$ (smooth functions), which is a strong condition to be guaranteed due to several artifacts arising from the physical experiment.

4. Equivalent Symmetry Condition

We consider that all frames (or projections) $u = u(\alpha, \beta)$ belong to a functional Hilbert space U (a second-order Sobolev space on a bounded domain $[-1, 1]^2$), with inner product $\langle u, u \rangle$ and inducing a norm $\|u\|^2 = \langle u, u \rangle$. As a first attempt, we search for the best functional approximation of the measured frame u_m on the subspace of functions satisfying John's condition. In this case, we want to solve the optimization problem

$$\begin{cases} \min & \phi(u) = \frac{1}{2}\|u - u_m\|^2 \\ \text{s.t.} & \mathcal{J}u = 0 \end{cases} \quad (10)$$

where $\mathcal{J}: U \rightarrow U$ is the linear functional describing John's consistency condition from Lemma 1. The first-order necessary conditions [15] for problem (10) guarantee the existence of a Lagrange multiplier $\lambda \in U$ such that $\langle \phi'(u), q \rangle + \langle \lambda, \mathcal{J}'(u)q \rangle = 0, \forall q \in U$. Using inner-product properties, we obtain

$$\langle \phi'(u), q \rangle + \langle \mathcal{J}'(u)^* \lambda, q \rangle = 0, \quad \forall q \in U \quad (11)$$

Here, $\mathcal{J}'(u)$ is the Frechét derivative of the functional form \mathcal{J} . The same applies to $\phi'(u)$. After realizing that $\phi'(u) = u - u_m$ and $\mathcal{J}'(u) = \mathcal{J}$, Equation (11) becomes $(u - u_m) + \mathcal{J}(u)^* \lambda = 0$. By imposing consistency, i.e., applying operator \mathcal{J} , it follows that $\mathcal{J}(u_m) - \mathcal{J}\mathcal{J}^* \lambda = 0$. Since \mathcal{J} is a differential operator, it is easy to see (using integration by parts) that $\mathcal{J}^* = \mathcal{J}$. Hence, $\mathcal{J}(u_m - \mathcal{J}\lambda) = 0$. As \mathcal{J} is not invertible (the kernel contains many functions different from the trivial solution), we have infinitely many solutions for this problem, which is a partial differential equation for the Lagrange multiplier λ . This comes from the fact that the set of functions satisfying $\mathcal{J} = 0$ is not closed on U . Hence, John's PDE does not provide any useful information with respect to the Lagrange multiplier λ , so we need another approach to compute an approximate solution.

To this aim, we denote H_u as the Hessian matrix of function u and define the nonlinear operator T by

$$T[u] = \text{Im}\left(\sqrt{\Delta[u]}\right) \quad (12)$$

where $\Delta[u]$ is the discriminant of the associated characteristic polynomial $p(\mu) = \det(H_u - \mu I)$ of the Hessian matrix H_u of function u . As is easy to note, p is a monic polynomial given by

$$p(\mu) = \mu^2 - \mu \text{tr}(u) + \det(u) \quad (13)$$

$$= \mu^2 - \mu(u_{\alpha\alpha} + u_{\beta\beta}) + (u_{\alpha\alpha}u_{\beta\beta} - u_{\beta\alpha}u_{\alpha\beta}) \quad (14)$$

where $\text{tr}(u)$ denotes the trace of the matrix H_u and $\det(u)$ is the determinant of H_u . The discriminant of p becomes

$$\Delta[u] = (u_{\alpha\alpha} + u_{\beta\beta})^2 - 4(u_{\alpha\alpha}u_{\beta\beta} - u_{\beta\alpha}u_{\alpha\beta}). \quad (15)$$

In this sense, we are replacing John's condition $\mathcal{J}(u) = 0$ with $T(u) = 0$. The following result indicates that both conditions are, in fact, the same.

Theorem 1. *If \mathbf{B} and \mathbf{C} are the sets defined by $\mathbf{B} = \{u \in U: \mathcal{J}(u) = 0\}$ and $\mathbf{C} = \{u \in U: T(u) = 0\}$, then $\mathbf{B} = \mathbf{C}$.*

Proof. The inclusion $\mathbf{B} \subset \mathbf{C}$ follows from the definitions. Let $u \in \mathbf{B}$, and then $\mathcal{J}(u) = 0$. The consistency condition determined by John's Equation (1) indicates that u must have all second derivatives everywhere in \mathbb{R}^2 and a symmetrical Hessian matrix. Therefore, H_u only has real eigenvalues $\{\mu_1, \mu_2\}$, i.e., the discriminant $\Delta[u]$ of p should be positive for all possible values of $z = (\alpha, \beta)$. The discriminant is non-negative if and only if the square root of the imaginary part of the discriminant is zero (i.e., $x > 0$ iff $\text{Im}\sqrt{x} = 0$). Necessity is straightforward, whereas sufficiency comes from taking $x = |x|e^{i\theta} = |x|(\cos\theta + i\sin\theta)$. The imaginary part of \sqrt{x} is $\sqrt{|x|}\sin\frac{\theta}{2}$, which is zero when $\theta = 2n\pi$ for $n \in \mathbb{N}$, i.e., $x = |x| > 0$). Then, $T(u) = 0$ and $\mathbf{B} \subset \mathbf{C}$.

Conversely, if $u \in \mathbf{C}$, then $T(u) = 0$. The Schwartz theorem requires u to be a C^2 function to verify $\mathcal{J}(u) = 0$, a property that we do not have here for function u . However, all partial derivatives $u_{\alpha\alpha}$, $u_{\alpha\beta}$, $u_{\beta\alpha}$ and $u_{\beta\beta}$ must exist everywhere to have $T(u) = 0$. An elegant result in [16] weakens the C^2 condition by requiring only the existence of all second derivatives, as is the case for u to have $\mathcal{J}(u) = 0$. Thus, $\mathbf{C} \subset \mathbf{B}$. \square

5. Smoothness Constraint for Coherent Diffraction Imaging

For coherent diffraction imaging (CDI) experiments, the wave hitting the sample propagates over long distances D (see Figure 1), with D much larger than the sample size. In this case, the measured data become the absolute squared value of the Fourier transform of the X-ray transform F . There are two main types of CDI experiments: the first is ptychography [17] and the second is plane-wave CDI [18] (among others, e.g., Bragg CDI). For both experiments, we aim to recover the X-ray transform image F , with the difference in the techniques being the number of shots used to illuminate the sample: one shot for plane-wave CDI and multiple shots for ptychography. The inversion algorithms are beyond the scope of this work but are widely discussed in the literature [19].

Ptychographic reconstructions can benefit from the overlapping data between adjacent measurements. In this sense, warm/hot pixels do not pose a significant challenge to the reconstruction scheme. In the CDI experiment, the measured data are represented by $\rho(w_\alpha, w_\beta) = |\hat{F}(w_\alpha, w_\beta)|$ (after taking the square root), where $\hat{\cdot}$ denotes the two-dimensional Fourier transform,

$$\hat{F}(w_\alpha, w_\beta) = \int_{\mathbb{R}^2} u(\alpha, \beta) e^{-2\pi i(\alpha w_\alpha + \beta w_\beta)} d\alpha d\beta \quad (16)$$

and u is defined by (4). Due to the fact that function u is a C^2 function (see Lemma 1), we can interchange the derivative with respect to w_α and w_β and the Fourier integral symbol, making it easy to demonstrate the following implication

$$\mathcal{J}(u) = 0 \Rightarrow \mathcal{J}(\hat{F}) = 0, \quad (17)$$

where each \mathcal{J} is computed in the respective domains of functions u and \hat{F} . Taking $\rho_\epsilon = \sqrt{\hat{F}^2 + \epsilon}$ for an arbitrarily small $\epsilon > 0$, it is easy to see that

$$\mathcal{J}(\rho) = \lim_{\epsilon \rightarrow 0} \mathcal{J}(\rho_\epsilon) = \lim_{\epsilon \rightarrow 0} \frac{1}{\sqrt{\hat{F}^2 + \epsilon}} \hat{F} \left[\frac{\partial^2 \hat{F}}{\partial w_\beta \partial w_\alpha} - \frac{\partial^2 \hat{F}}{\partial w_\alpha \partial w_\beta} \right] = \lim_{\epsilon \rightarrow 0} \frac{\hat{F}}{\sqrt{\hat{F}^2 + \epsilon}} \mathcal{J}(\hat{F}) = 0 \quad (18)$$

Hence, the diffraction pattern data also satisfy the symmetry condition imposed by the commutator \mathcal{J} . In this sense, we can also apply the operator T to the coherent diffraction image data ρ , i.e., $T(\rho) = 0$, as indicated in Theorem 1.

Inversion and smoothness: One of the most celebrated phase-retrieval strategies is the HIO (hybrid input–output [5]) method, which uses a shrink-wrap strategy. Typically, it builds a Gaussian blurred version of the iterates in order to *shrink* the support of the sample, making the convergence of the iterations easier. The same shrink-wrap strategy can be used with the RAAR (relaxed averaged alternating reflections [20]) algorithm. The OSS (oversampling smoothness [6]) algorithm enforces smoothness via Gaussian blurring on the iterates outside the support of the sample, compensating for high frequencies and noise in the data. Without going into the details of these methods, we observe that the symmetry condition demonstrated by Equation (18) naturally requires smoothness in the data, which implies imposing smoothness on the sample. Using the notation provided in the introduction, if f is the sample, then

$$\mathcal{J}(\rho) \neq 0 \Rightarrow f \notin C^2 \quad (19)$$

The above negation justifies why smoothness is typically used in inversion schemes for phase recovery. Also, as far as we know, the operator T (Equation (12)) has not been previously used in any inversion scheme. Since the development of inversion algorithms for the phase is beyond the scope of this work, we only point out that T can be used in either the object domain (as used in the celebrated algorithms) or the data domain.

Correcting measured data: The symmetry condition $\mathcal{J}(\rho) = 0$ (or, equivalently, $T(\rho) = 0$) can be used to find numerical inconsistencies in the measured data. In fact, some outliers are present in the measured diffraction pattern due to the photon-counting nature of the detector. These outliers are typically known as hot/warm pixels and can strongly affect the convergence of the aforementioned phase-retrieval strategies; hence, they have to be masked out from the original data. These outliers are introduced in the data as a rectangular function supported within one pixel, thus removing differentiability from the (expected) C^2 diffraction data. We can mask the outliers from a smooth image using the conventional strategy

$$\rho^*(t) = a \iff |\rho(t) - \mu[\rho]| > m \sigma[\rho], \quad (20)$$

for all pixels t , where $\mu[\rho]$ and $\sigma[\rho]$ are the mean and standard deviation of the image ρ , respectively. The choice of m can be defined previously for the image ρ . The value of a can be chosen arbitrarily, for instance, as a negative constant, to distinguish between measured and unknown values. For large arrays defining the measured data ρ , a splitting strategy can be used to apply (20) throughout small domain batches of ρ . We denote by \mathcal{B}_n the batch strategy for cleaning ρ with $n \times n$ regular subdomains and using the constant m , as defined in (20). The composition of \mathcal{B}_n , that is,

$$\rho^* = \mathcal{B}_n^c[\rho], \quad 1 \leq c \in \mathbb{Z} \quad (21)$$

provides us with the corrected data, which can be used as input for different imaging techniques.

In practice, due to hardware instrumentation, it is also important to know the exact location of outliers prior to removing them. This can help us better understand the hardware specifications and improve them. Since ρ must be a smooth function, we use $T(\rho) = 0$ as an indicator to identify outliers by setting a mask function M in the following manner

$$M(t) = \begin{cases} 1, & |T(\rho)(t) - T(\rho^*)(t)| > 0 \\ 0, & \text{otherwise} \end{cases} \quad (22)$$

where $T(\rho) = \text{Im}(\sqrt{\Delta[\rho]})$, as defined in (12). The above support function can be updated at each application of \mathcal{B}_n , as some outliers are eventually not detected.

In order to use an iterative method to improve the global image function u , which does not satisfy $T(u) = 0$, we can use a Newton strategy applied within a Hilbert space setting, i.e., we look for a sequence $\{u_k\}$ defined by

$$u_{k+1} = u_k + q_k, \quad T'(u_k) \cdot q_k = -T(u_k) \tag{23}$$

where T' is the Fréchet derivative of T at the point u_k acting on the step function q_k , as described in the following Lemma.

Lemma 2. *The nonlinear functional T , defined in (12), is Fréchet differentiable. The first Fréchet derivative $T'(u)$ acting on $q \in U$ is the linear operator*

$$T'(u) \cdot q = -\frac{T(u)}{|Z(u)|^2} [\text{tr}(u)\text{tr}(q) - 2(u_{\alpha,\alpha}q_{\beta,\beta} + q_{\alpha,\alpha}u_{\beta,\beta} - u_{\beta,\alpha}q_{\alpha,\beta} - q_{\beta,\alpha}u_{\alpha,\beta})] \tag{24}$$

where $\text{tr}(u)$ denotes the trace for the Hessian matrix of u , Δ represents the discriminant in (15), and $Z(u) = \sqrt{\Delta(u)}$.

Proof. For simplicity, let us denote $\det(u) = \det(H_u)$, where H_u is the Hessian of u . It follows that

$$\begin{aligned} T(u + q) &= \text{Im}\sqrt{\Delta[u + q]} \\ &= \text{Im}\left\{[\text{tr}(u) + \text{tr}(q)]^2 - 4Q_1\right\}^{1/2} \\ &= \text{Im}\left\{\text{tr}(u)^2 + 2\text{tr}(u)\text{tr}(q) + \text{tr}(q)^2 - 4Q_1\right\}^{1/2} \end{aligned} \tag{25}$$

Here, Q_1 is defined as

$$\begin{aligned} Q_1 &= (u_{\alpha,\alpha} + q_{\alpha,\alpha})(u_{\beta,\beta} + q_{\beta,\beta}) - (u_{\beta,\alpha} + q_{\beta,\alpha})(u_{\alpha,\beta} + q_{\alpha,\beta}) \\ &= u_{\alpha,\alpha}u_{\beta,\beta} + u_{\alpha,\alpha}q_{\beta,\beta} + q_{\alpha,\alpha}u_{\beta,\beta} + q_{\alpha,\alpha}q_{\beta,\beta} \\ &\quad - u_{\beta,\alpha}u_{\alpha,\beta} - u_{\beta,\alpha}q_{\alpha,\beta} - q_{\beta,\alpha}u_{\alpha,\beta} - q_{\beta,\alpha}q_{\alpha,\beta} \end{aligned} \tag{26}$$

Returning to (25), we obtain $T(u + q) = \text{Im}\{\Delta[u] + Q_2 + Q_3\}^{1/2}$, with Q_2 given by

$$\begin{cases} Q_2 = [2\text{tr}(u)\text{tr}(q) - 4\{u_{\alpha,\alpha}q_{\beta,\beta} + q_{\alpha,\alpha}u_{\beta,\beta} - u_{\beta,\alpha}q_{\alpha,\beta} - q_{\beta,\alpha}u_{\alpha,\beta}\}] \\ Q_3 = [\text{tr}(q)^2 - 4\det(H_q)] \end{cases} \tag{27}$$

where H_q is the Hessian matrix of function q . We use the fact that $\text{Im}(1/z) = -\text{Im}(z)/|z|^2$ for any complex number $z \neq 0$. Also, since Q_2 and Q_3 are real numbers, we can use the first-order expansion $\sqrt{x + h} = \sqrt{x} + \frac{1}{2\sqrt{x}}h + O(h^2)$ to obtain

$$T(u + q) = \text{Im}\left\{\sqrt{\Delta[u]} + \frac{1}{2\sqrt{\Delta[u]}}(Q_2 + Q_3) + O([Q_2 + Q_3]^2)\right\} \tag{28}$$

$$= \text{Im}\sqrt{\Delta[u]} - \frac{\text{Im}\sqrt{\Delta[u]}}{|\sqrt{\Delta[u]}|^2} \left(\frac{Q_2}{2} + \frac{Q_3}{2}\right) + O([Q_2 + Q_3]^2) \tag{29}$$

Thus, taking $M(u) = -T(u)/2|\sqrt{\Delta(u)}|^2$, it follows that

$$T(u + q) - T(u) - M(u)Q_2 - M(u)Q_3 = O([Q_2 + Q_3]^2) \tag{30}$$

Since u is a smooth function on a compact set Ω , we can assume that its second-order partial derivatives are bounded, and a simple application of the Plancherel theorem shows that $\|Q_3\|/\|q\| \rightarrow 0$ and $\|(Q_2 + Q_3)^2\|/\|q\| \rightarrow 0$ as $\|q\| \rightarrow 0$. Hence, $M(u)Q_2$ is the first Fréchet derivative of T . \square

From (24), we know that for functions u not satisfying $T(u) = 0$, we can find the Newton direction q_k from (23), solving the following parabolic partial differential equation

$$\text{tr}(u)\text{tr}(q) - 2(u_{\alpha,\alpha}q_{\beta,\beta} + q_{\alpha,\alpha}u_{\beta,\beta} - u_{\beta,\alpha}q_{\alpha,\beta} - q_{\beta,\alpha}u_{\alpha,\beta}) = |Z(u)|^2 \quad (31)$$

or, equivalently,

$$u_{\alpha,\alpha}[q_{\beta,\beta} - q_{\alpha,\alpha}] + 2[u_{\beta,\alpha}q_{\alpha,\beta} + q_{\beta,\alpha}u_{\alpha,\beta}] = |Z(u)|^2 \quad (32)$$

Finding an appropriate finite-element strategy for the above partial differential equation is beyond the scope of this work. Appropriate boundary conditions can be imposed on this problem in order to find a numerical solution for function q_k [21]. For instance, we can impose Dirichlet conditions on the neighborhood of each pixel. This can be achieved using different functions, such as a Gaussian kernel with an appropriate full width at half maximum (FWHM).

6. Discussion

To illustrate our methodology, we present a radiographic projection recovered using the ptychography technique [22] with data collected at the fourth-generation Brazilian Synchrotron beamline CATERETE [23]. The measurements were taken at a distance of 14m with an energy of 3.8 KeV. The phase image recovered through ptychography from a sequence of diffraction patterns is presented in Figure 2a. Here, the projection is expected to be an X-ray transform, as defined in Equation (1), and thus should be sufficiently smooth. This particular sample refers to a small glass sphere with an approximate diameter of 8.5 μm , where the jump from one phase to another (e.g., air to material) is not sharp but is twice differentiable. Hence, we expect to obtain T numerically close to zero. In order to compute the operator T in (12) on a digital grid, a central finite difference scheme is used for $u_{\alpha\alpha}$ and $u_{\beta\beta}$, a forward-forward scheme is used for $u_{\alpha\beta}$, and a backward-backward scheme is used for $u_{\beta\alpha}$. Figure 2b presents the effect of operator T on the imaging grid, where points with $T = 0$ are shown in yellow and those with other values are shown in blue.

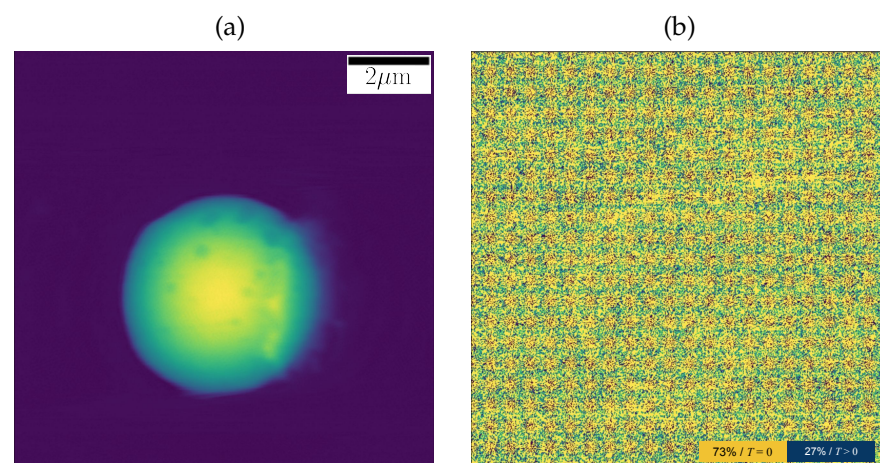


Figure 2. An example of parallel X-ray projections (a) and the action of operator T (b). The X-ray projection was recovered from the sequence of diffraction patterns using a ptychographic technique.

The outlier analysis of a diffraction pattern has to take into account the fact that the intensity tends to zero for high frequencies, as predicted by the Riemman–Lebesgue Lemma [24]. Therefore, when analyzing small portions of the diffraction pattern, we must consider the sparsity of the selected subimage to avoid mistaking outliers for the signal

itself. For this, we use the Hoyer sparsity measure [25], i.e., we use the following function s as the sparsity indicator

$$s(z) = \frac{\sqrt{k} - \frac{\|z\|_1}{\|z\|_2}}{\sqrt{k} - 1}, \quad m(z) = \begin{cases} 5, & s(z) \leq 0.6 \\ 8, & s(z) > 0.6 \end{cases}, \quad z \in \mathbb{R}^k, \quad (33)$$

where the value of $s \leq 0.6$ indicates the need for the outlier removal procedure (20), as determined by m in the above equation. Figure 3 presents two examples of 256×256 subimages extracted from a single original 3072×3072 diffraction pattern, indicated in (a.1) and (b.1). As discussed, there are several outliers in the selected original subimages, which disrupt the smoothness of the data. We can observe in Figure 3a.1,a.2 that hot/warm pixels do not have the same intensities and are not considered defective pixels in the sense that they contain recorded information. The circles marked by dotted circles in image (a.1) highlight outlier pixels with different recorded intensities (low and high). Using an 8×8 grid, we compute the sparsity using (33) and the masks from (20) to identify outliers, presented in (b.1) and (b.2), from which clean images are straightforwardly obtained, as shown in (a.3) and (b.3). Null values in the colormap visually identify outlier pixels in the original dataset.

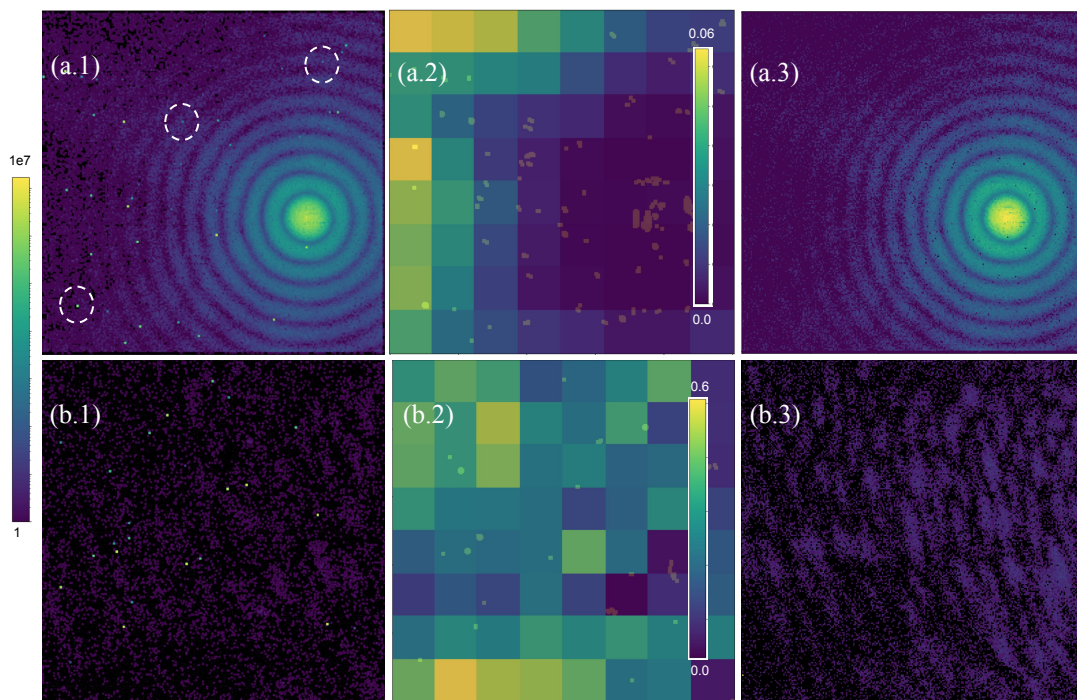


Figure 3. Two examples of a real diffraction pattern are presented in (a.1) and (b.1), with several outliers indicated by white dotted circles. Figures (a.2) and (b.2) present the sparsity map using a 8×8 , where the mask function from Equation (22) is applied. Figures (a.3) and (b.3) show the corrected diffraction patterns.

A numerical example of CDI is presented in Figure 4, where a coherent diffraction pattern of a compactly supported two-dimensional square function is shown. The diffraction dataset was corrupted with a low (i.a) and high (ii.a) number of hot/warm pixels. The application of the aforementioned removal strategy yields the results presented in Figure 4i.b,ii.b, where hot/warm pixels are clearly identified and masked by white values. The reconstructions—obtained through shrink-wrap HIO—are presented in Figure 4i.c without correction and Figure 4i.d with correction, respectively. It is clear that for a low number of hot/warm pixels, conventional HIO can still converge to a feasible solution, even though this solution has much more noise in the background compared to the recon-

struction obtained after cleaning the input dataset using the proposed strategy. The same strategy is presented in (ii.c) and (ii.d). Now, the HIO was not able to properly converge to a reconstructed solution, whereas the cleaned input dataset (ii.b) could be used to obtain an optimal reconstruction (ii.d).

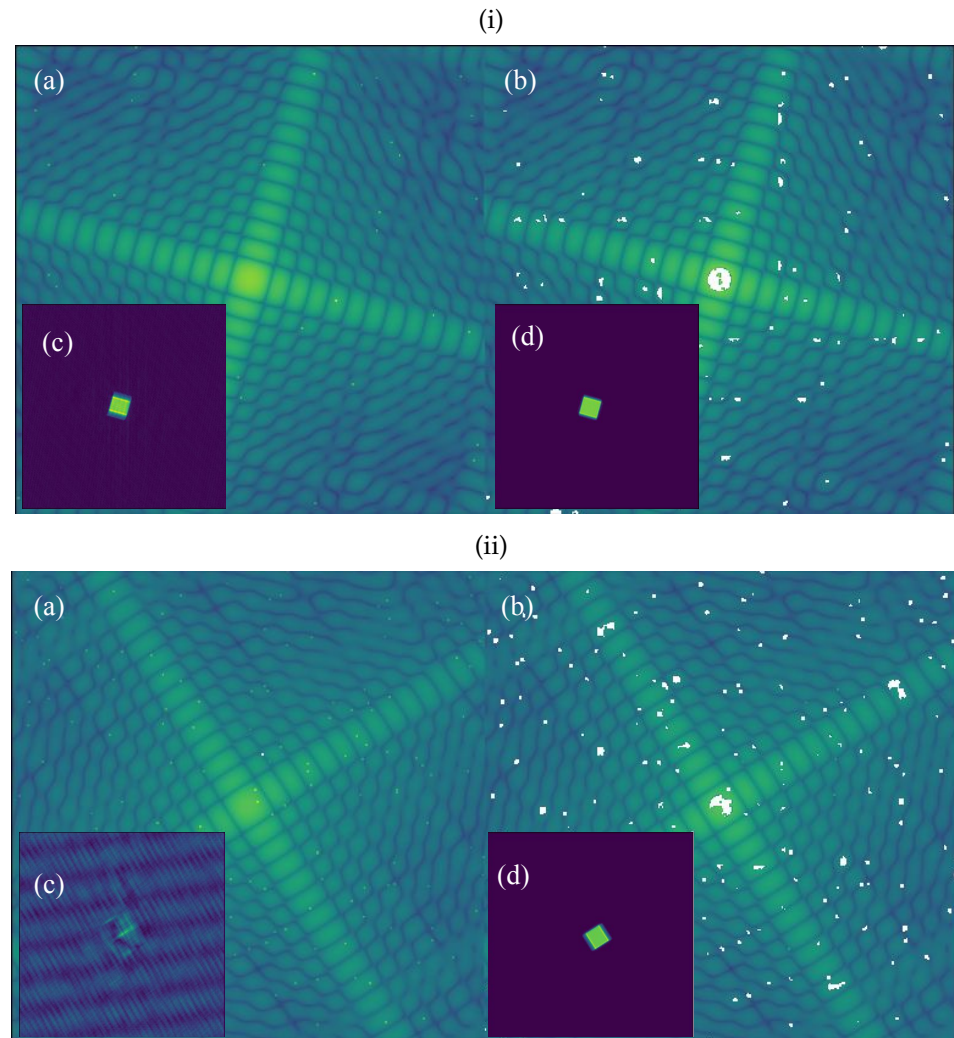


Figure 4. Simulated example for the diffraction pattern of a compactly supported two-dimensional square function. A low (i.a) and high (ii.a) number of hot/warm pixels are corrupting the original dataset. The cleaned dataset, using the methodology proposed in this manuscript, is presented in (i.b,ii.b) (white values surrounding problematic pixels). The reconstructed dataset using the HIO algorithm is presented in (i.c)/(ii.c) (without corrected data) and (i.d)/(ii.d) (with corrected data).

7. Conclusions and Further Research

Experiments that deal with the projection of a sample represent an important portion of scientific cases in X-ray imaging research. Often, projections are not measured directly but are obtained after phase-retrieval algorithms are applied to the measured data. These algorithms solve an inverse problem that strongly depends on the quality of the measured data, which can be corrupted by noise and defective pixels. In this work, we have demonstrated the existence of an operator that enforces the smoothness for both the data and the phase-retrieved projections. In this manner, we are able to easily identify pixels that should be ignored for violating such smoothness conditions. The method can not only qualitatively indicate image quality but also aid scientists in quickly preparing their data for phase-retrieval algorithms.

Author Contributions: Conceptualization, E.X.M.; software, T.K.; validation, Y.R.T.; formal analysis, E.X.M.; investigation, E.X.M.; writing—original draft preparation, E.X.M.; writing—review and editing, T.K. and Y.R.T.; project administration, E.X.M. All authors have read and agreed to the published version of the manuscript.

Funding: This research received no external funding.

Data Availability Statement: No new data were created for this article. The dataset used in this manuscript was kindly provided by Florian Meneau and Carla Polo [23]. The implementation of the method was carried out using conventional Python numerical packages running on Jupyter notebooks. The notebook can be made available upon request.

Acknowledgments: We would like to acknowledge the Brazilian Ministry of Science, Technology, and Innovation (MCTI) for supporting this work through the Brazilian Center for Research in Energy and Materials (CNPEM). The real dataset was kindly provided by Florian Meneau and Carla Polo from the coherent diffraction imaging beamline CATERETÉ at Sirius (the fourth-generation Brazilian Synchrotron).

Conflicts of Interest: The authors declare no conflicts of interest.

References

1. Miao, J.; Ishikawa, T.; Robinson, I.K.; Murnane, M.M. Beyond crystallography: Diffractive imaging using coherent X-ray light sources. *Science* **2015**, *348*, 530–535. [[CrossRef](#)] [[PubMed](#)]
2. Liu, L.; Alves, M.; Arroyo, F.; Brunheira, G.; Cruz, G.; Giachero, A.; Oliveira, A.; de Oliveira, F.; Ramirez, G.; Resende, X.; et al. Status of SIRIUS operation with users. In Proceedings of the 14th International Particle Accelerator Conference, IPAC-2023, Venice, Italy, 7–12 May 2023.
3. Tavares, P.F.; Leemann, S.C.; Sjöström, M.; Andersson, Å. The MAX IV storage ring project. *J. Synchrotron Radiat.* **2014**, *21*, 862–877. [[CrossRef](#)] [[PubMed](#)]
4. Chaize, J.M.; Bourtembourg, R.; Götz, A.; Poncet, F.; Pons, J.; Taurel, E.; Verdier, P.; Tappret, N. The ESRF Extremely Brilliant Source—A 4th Generation Light Source. In Proceedings of the Proceedings, 16th International Conference on Accelerator and Large Experimental Physics Control Systems, ICALEPCS, Barcelona, Spain, 8–13 October 2017; pp. 8–13.
5. Fienup, J.R. Phase retrieval algorithms: A comparison. *Appl. Opt.* **1982**, *21*, 2758–2769. [[CrossRef](#)] [[PubMed](#)]
6. Rodriguez, J.A.; Xu, R.; Chen, C.C.; Zou, Y.; Miao, J. Oversampling smoothness: An effective algorithm for phase retrieval of noisy diffraction intensities. *J. Appl. Crystallogr.* **2013**, *46*, 312–318. [[CrossRef](#)] [[PubMed](#)]
7. Marchesini, S.; He, H.; Chapman, H.N.; Hau-Riege, S.P.; Noy, A.; Howells, M.R.; Weierstall, U.; Spence, J.C. X-ray image reconstruction from a diffraction pattern alone. *Phys. Rev. B* **2003**, *68*, 140101. [[CrossRef](#)]
8. Ju, F.; Sun, Y.; Gao, J.; Hu, Y.; Yin, B. Image outlier detection and feature extraction via L1-norm-based 2D probabilistic PCA. *IEEE Trans. Image Process.* **2015**, *24*, 4834–4846. [[CrossRef](#)] [[PubMed](#)]
9. Huang, H.; Yuan, E.; Zhang, D.; Sun, D.; Yang, M.; Zheng, Z.; Zhang, Z.; Gao, L.; Panezai, S.; Qiu, K. Free field of view infrared digital holography for mineral crystallization. *Cryst. Growth Des.* **2023**, *23*, 7992–8008. [[CrossRef](#)]
10. Barrett, H.H.; Swindell, W. *Radiological Imaging: The Theory of Image Formation, Detection, and Processing*; Academic Press: Cambridge, MA, USA, 1996; Volume 2.
11. John, F. The ultrahyperbolic differential equation with four independent variables. *Fritz John Collect. Pap.* **1985**, *1*, 79.
12. Ma, J.; Wu, S.; Qi, H.; Li, B.; Yan, H.; Zhou, L.; Xu, Y. John’s equation-based consistency condition and corrupted projection restoration in circular trajectory cone beam CT. *Sci. Rep.* **2017**, *7*, 4920. [[CrossRef](#)] [[PubMed](#)]
13. Kudo, H.; Rodet, T.; Noo, F.; Defrise, M. Exact and approximate algorithms for helical cone-beam CT. *Phys. Med. Biol.* **2004**, *49*, 2913. [[CrossRef](#)] [[PubMed](#)]
14. Patch, S.K. Consistency conditions upon 3D CT data and the wave equation. *Phys. Med. Biol.* **2002**, *47*, 2637. [[CrossRef](#)] [[PubMed](#)]
15. Luenberger, D.G. *Optimization by Vector Space Methods*; John Wiley & Sons: Hoboken, NJ, USA, 1997.
16. Tolstov, G.P. On partial derivatives. *Izv. Ross. Akad. Nauk. Seriya Mat.* **1949**, *13*, 425–446.
17. Pfeiffer, F. X-ray ptychography. *Nat. Photonics* **2018**, *12*, 9–17. [[CrossRef](#)]
18. Chapman, H.N.; Barty, A.; Marchesini, S.; Noy, A.; Hau-Riege, S.P.; Cui, C.; Howells, M.R.; Rosen, R.; He, H.; Spence, J.C.; et al. High-resolution ab initio three-dimensional X-ray diffraction microscopy. *JOSA A* **2006**, *23*, 1179–1200. [[CrossRef](#)] [[PubMed](#)]
19. Liu, Y.; Chen, B.; Li, E.; Wang, J.; Marcelli, A.; Wilkins, S.; Ming, H.; Tian, Y.; Nugent, K.; Zhu, P.; et al. Phase retrieval in X-ray imaging based on using structured illumination. *Phys. Rev. A* **2008**, *78*, 023817. [[CrossRef](#)]
20. Luke, D.R. Relaxed averaged alternating reflections for diffraction imaging. *Inverse Probl.* **2004**, *21*, 37. [[CrossRef](#)]
21. Kılıçman, A.; Eltayeb, H. Note on partial differential equations with non-constant coefficients and convolution method. *Appl. Math. Inf. Sci.* **2012**, *6*, 59–63.
22. Baraldi, G.L.; Dias, C.S.; Silva, F.M.; Tolentino, H.C.; Miqueles, E.X. Fast reconstruction tools for ptychography at Sirius, the fourth-generation Brazilian synchrotron. *J. Appl. Crystallogr.* **2020**, *53*, 1550–1558. [[CrossRef](#)]

23. Meneau, F.; Passos, A.; Garcia, P.; Vinaches, P.; Manoel, L.; Kalile, T.; Zerba, J.; Rodrigues, G.; Miqueles, E.; Baraldi, G.; et al. Cateretê: The Coherent X-ray Scattering Beamline at the 4th generation synchrotron facility SIRIUS. *Acta Crystallogr. Sect. A Found. Adv.* **2021**, *77*, C283. [[CrossRef](#)]
24. Bochner, S.; Chandrasekharan, K. *Fourier Transforms*; Princeton University Press: Princeton, NJ, USA, 1949; Number 19.
25. Hurley, N.; Rickard, S. Comparing measures of sparsity. *IEEE Trans. Inf. Theory* **2009**, *55*, 4723–4741. [[CrossRef](#)]

Disclaimer/Publisher’s Note: The statements, opinions and data contained in all publications are solely those of the individual author(s) and contributor(s) and not of MDPI and/or the editor(s). MDPI and/or the editor(s) disclaim responsibility for any injury to people or property resulting from any ideas, methods, instructions or products referred to in the content.